

Supporting Information for

Unlocking the Potential of Nanoparticles Composed of Immiscible Elements for Direct H₂O₂ Synthesis

Donghun Kim,^{1,†} Hyobin Nam,^{2,3,†} Young-Hoon Cho,^{4,†} Byung Chul Yeo,^{1,†} So-Hye Cho,² Jae-Pyoung Ahn,^{5,*} Kwan-Young Lee,^{4,*} Seung Yong Lee,^{2,3,*} and Sang Soo Han^{1,*}

¹Computational Science Research Center, Korea Institute of Science and Technology, Seoul 02792, Republic of Korea

²Materials Architecturing Research Center, Korea Institute of Science and Technology, Seoul 02792, Republic of Korea

³Department of Nanomaterials Science and Engineering, Korea University of Science and Technology, Daejeon 34113, Republic of Korea

⁴Department of Chemical and Biological Engineering, Korea University, Seoul 02841, Republic of Korea

⁵Advanced Analysis Center, Korea Institute of Science and Technology, Seoul 02792, Republic of Korea

*Correspondence to: sangsoo@kist.re.kr (S.S.H); patra@kist.re.kr (S.Y.L); kylee@korea.ac.kr (K.-Y.L); jpahn@kist.re.kr (J.-P. A).

†These authors contributed equally to this work.

Table S1. Information of used catalyst weight (mg), and composition (A:B ratio) for each catalyst sample.

Catalyst (AB)		Used Catalyst weight (mg)	Ratio of initial loading (A:B)	Real catalytic ratio A:B (from ICP measurements)
Rh		3.0	-	-
Ag		2.1	-	-
Pt		1.4	-	-
Pd		3.9	-	-
Ir		4.9	-	-
Au		9.6	-	-
RhAg	Rh₁₃Ag₈₇	5.8	10:90	13:87
	Rh₂₆Ag₇₄	6.5	30:70	26:74
	Rh₅₀Ag₅₀	6.1	65:35	50:50
	Rh₆₉Ag₃₁	4.9	80:20	69:31
RhAu	Rh₄₆Au₅₄	6.6	50:50	46:54
PtAu	Pt₈Au₉₂	1.7	10:90	8:92
	Pt₂₈Au₈₂	1.7	30:70	28:72
	Pt₄₂Au₅₈	1.7	50:50	42:58
IrAg	Ir₁₈Ag₈₂	2.0	50:50	18:82
IrAu	Ir₁₀Au₉₀	8.6	50:50	10:90

Table S2. The energetics of each O₂ and H₂ dissociative adsorption on the (111) surfaces of six pure metals (Ag, Au, Ir, Rh, Pt, and Pd). Our values were all obtained from the revised PBE functional, whereas the references utilized PBE one^{S1,S2} or PW91^{S3,S4,S5}.

	O ₂ dissociation		H ₂ dissociation	
	E (O ₂ [*] → 2O [*])	E _a (O ₂ [*] → 2O [*])	E (H ₂ [*] → 2H [*])	E _a (H ₂ [*] → 2H [*])
Ag	+0.26 (+0.19 ^{S3})	1.15 (1.04 ^{S3})	+0.76	1.71
Au	+0.71 (+0.74 ^{S3})	2.09 (1.90 ^{S3})	+0.58 (+0.50 ^{S2})	1.29 (1.09 ^{S2})
Ir	-2.06 (-1.92 ^{S4})	0.18 (0.06 ^{S4})	-0.51 (-0.81 ^{S2})	0.22 (0.46 ^{S2})
Rh	-2.35	0.23	-0.54	0.02
Pt	-1.39	0.70 (0.73 ^{S2})	-0.42 (-0.87 ^{S2})	0.17 (0.03 ^{S2})
Pd	-1.66 (-1.93 ^{S1}) (-2.08 ^{S5})	1.10 (0.97 ^{S1}) (0.51 ^{S5})	-0.92 (-1.06 ^{S1})	0.17 (0.05 ^{S1})

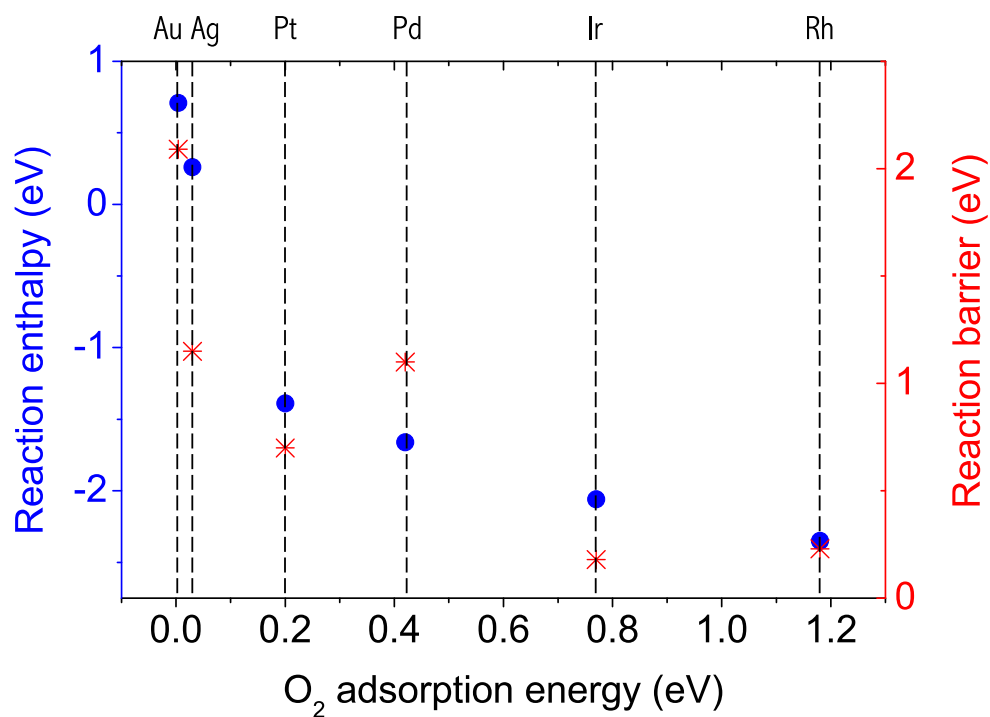


Fig. S1. Correlation between O_2 dissociation energetics (reaction enthalpy or barrier) and O_2 adsorption energy for the various metals investigated in this work. The stronger the O_2 molecules are adsorbed on the metal surface, the more easily the O_2 molecules are dissociated into atomic species.

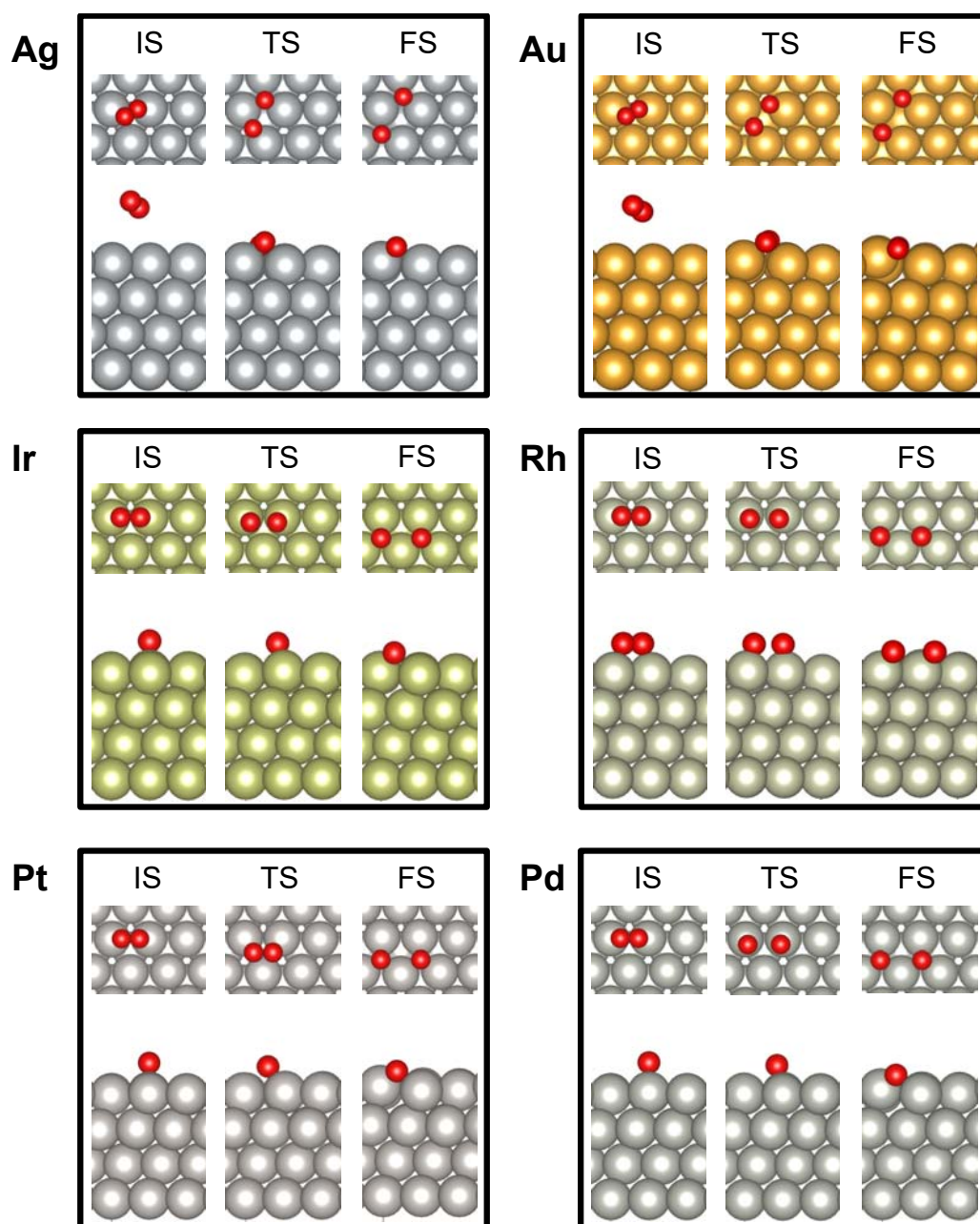


Fig. S2. The geometries of the O_2 dissociative adsorptions on the (111) surfaces of six pure metals (Ag, Au, Ir, Rh, Pt, and Pd). Each material set consists of top- and side-view geometries of the initial state (IS), transition state (TS), and final state (FS). Red spheres represent oxygen atoms, and other colors represent metal atoms in the investigation.

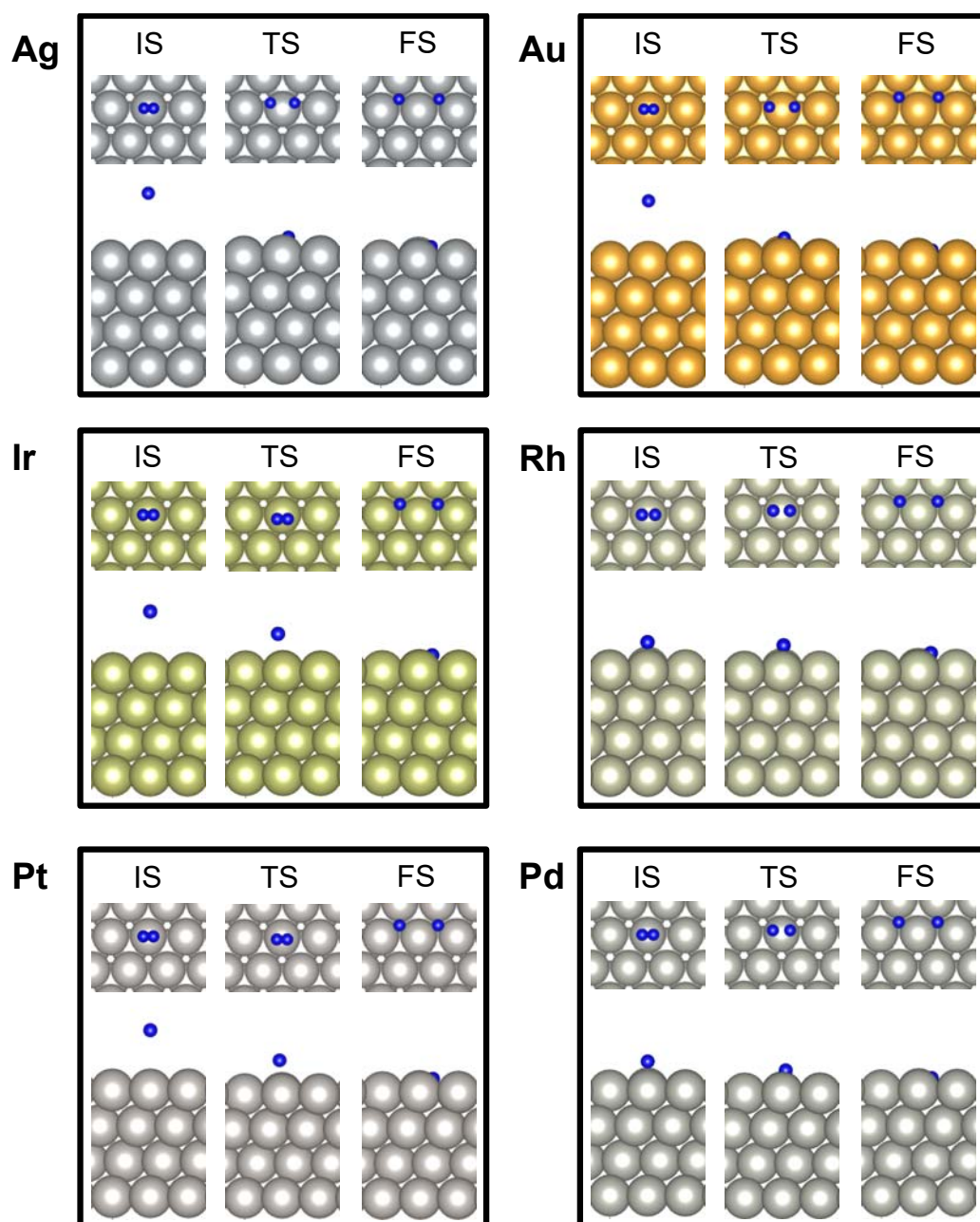
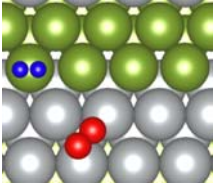
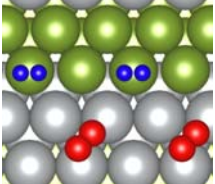
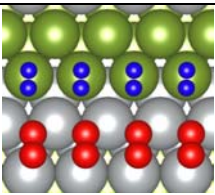


Fig. S3. The geometries of the H_2 dissociative adsorptions on the (111) surfaces of six pure metals (Ag, Au, Ir, Rh, Pt, and Pd). Each material set consists of top- and side-view geometries of the initial state (IS), transition state (TS), and final state (FS). Blue spheres represent hydrogen atoms, and other colors represent metal atoms in the investigation.

Table S3. Migration barriers of O₂ and H₂ molecules between Rh and Ag domains. Both O₂ and H₂ molecules energetically prefer migrating toward Rh domains (Ag→Rh), compared to the other way (Rh→Ag). These results may seemingly contradict with our initial geometry set-up of O₂ and H₂ molecules, i.e., O₂ (Ag)–H₂ (Rh) configuration. This can, however, be justified from a kinetics viewpoint. It is well known that H₂ molecules diffuse toward the catalyst surfaces much faster than O₂ molecules do due to their smaller masses, approximately 4 times faster given the relation of “Diffusivity $\propto \frac{1}{\sqrt{m}}$ ” (m =particle mass, $m_{\text{Oxygen}}=16$, $m_{\text{Hydrogen}}=1$)^{S6}. As a result, exposed Rh domains are predominantly covered by H₂ molecules. At such a circumstance of Rh domains being H₂-dominated, O₂ molecules would reach to Ag domains, causing O₂ (Ag)–H₂ (Rh) configurations to most likely occur, particularly in the early stages of the O₂/H₂ mixture feed.

	Barrier E_a for O₂	Barrier E_a for H₂
Rh→Ag	0.57 eV	0.51 eV
Ag→Rh	0.09 eV	0.14 eV

Table S4. Adsorption energies of O₂-H₂ pair at different surface coverages. Coverages are shown both in % unit, and in O₂-H₂ pair #/nm² unit. Since our DFT model adopted the initial configurations of O₂ (Ag)-H₂ (Rh), we calculated the adsorption energy per O₂-H₂ pair at three surface coverages of 25% (current model), 50%, and 100%. The average adsorption energy is similarly low (-0.37 eV) at 25% and 50%; however, it is higher (-0.22 eV) at the denser coverage of 100% due to stronger molecular interactions; thus, our choice of 25% coverage in the DFT model is reasonable.

Image	Surface coverage (%) (O ₂ -H ₂ pair #/nm ²)	Adsorption energy (eV) per O ₂ -H ₂ pair
	25% (0.90)	-0.37
	50% (1.81)	-0.36
	100% (3.61)	-0.22

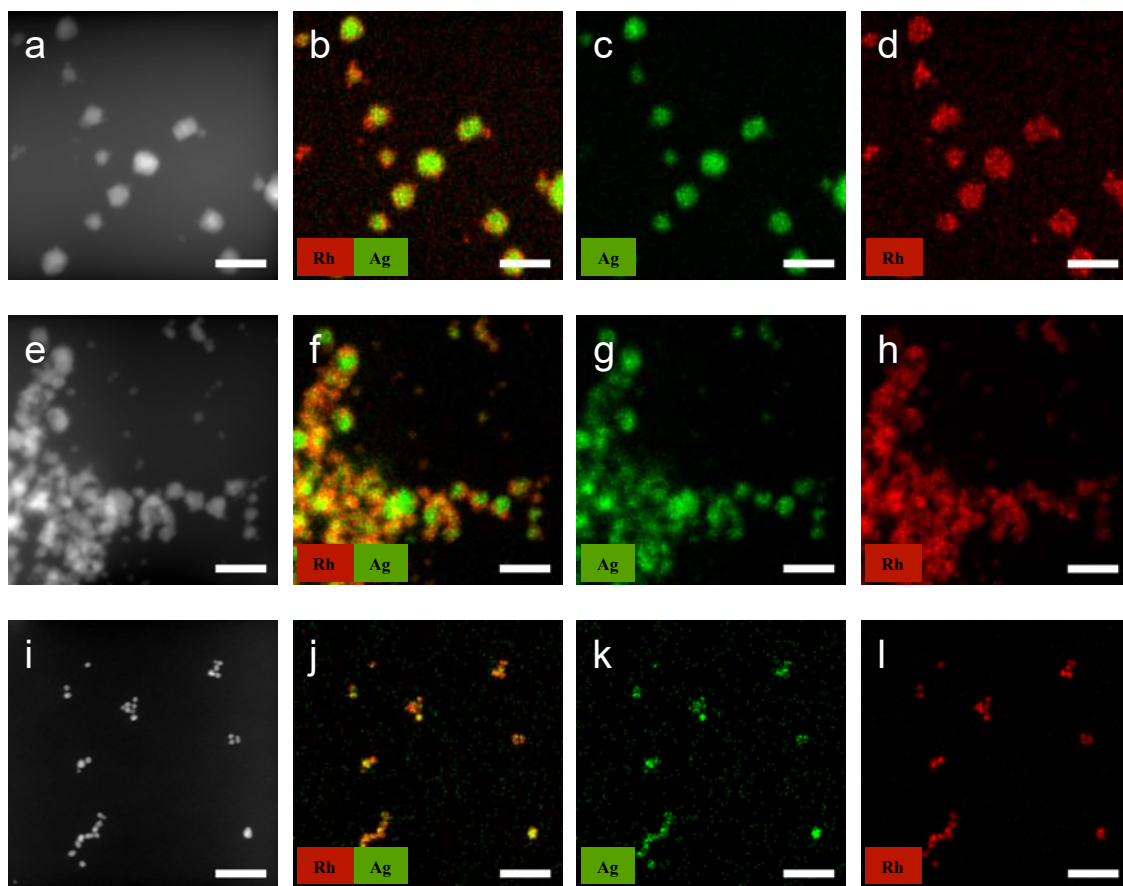
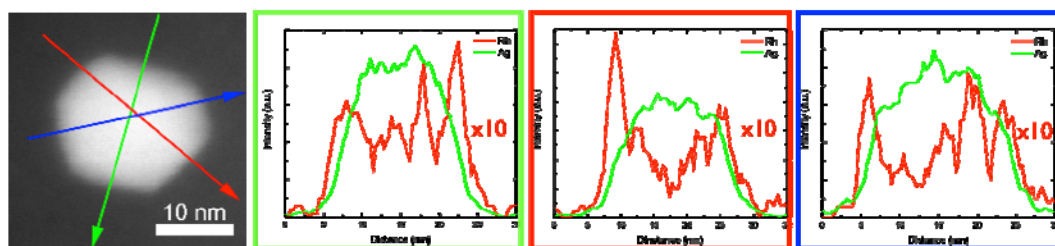


Fig. S4. Structural analysis of the RhAg NPs with different compositions. The representative HAADF grayscale image and EDS (RGB) maps of the collective (a-d) Rh₂₆Ag₇₄, (e-h) Rh₅₀Ag₅₀, and (i-l) Rh₆₉Ag₃₁ NPs. Scale bars in the images and maps represent 20 nm.

(A) Rh₁₃Ag₈₇ NPs (our sample)



(B) Rh₂₆Ag₇₄ NPs (our sample)

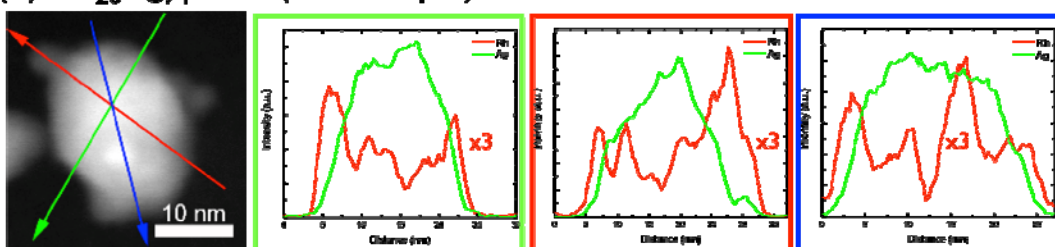
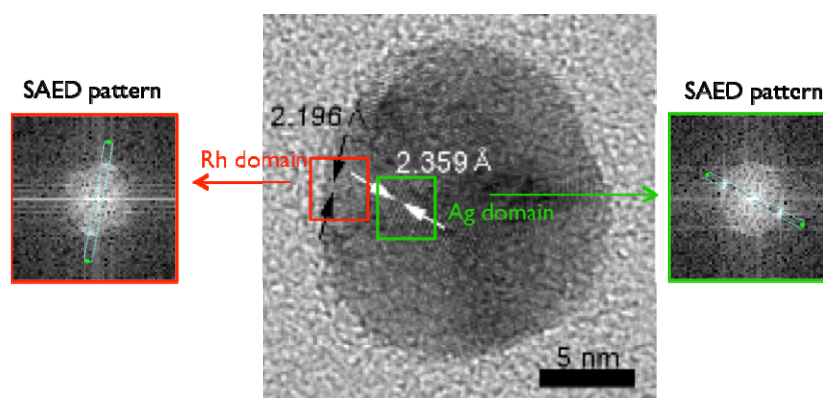


Fig. S5. EDS line-scan images of our RhAg NPs. (A) line-scan images of Rh₁₃Ag₈₇ NPs (Rh profile $\times 10$ amplified, for clarity). (B) line-scan images of Rh₂₆Ag₇₄ NPs (Rh profile $\times 3$ amplified, for clarity). A prominent difference between Ag and Rh profiles is observed: Ag profiles are Gaussian-distribution-like, whereas Rh profiles irregularly fluctuate. This result is consistent with our claim on NP structure that Ag forms the core of NPs and Rh islands of different sizes sit on the Ag cores in a random manner.

(A) Rh₁₃Ag₈₇ NPs



(B) Rh₂₆Ag₇₄ NPs

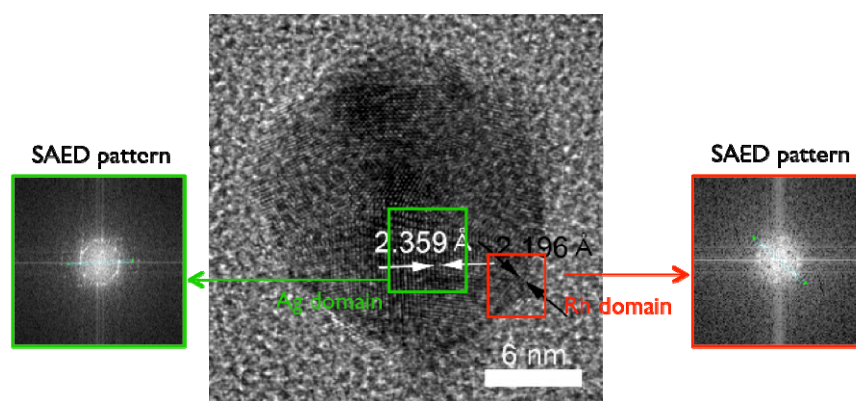


Fig. S6. SAED pattern analysis of (A) Rh₁₃Ag₈₇ NPs and (B) Rh₂₆Ag₇₄ NPs.

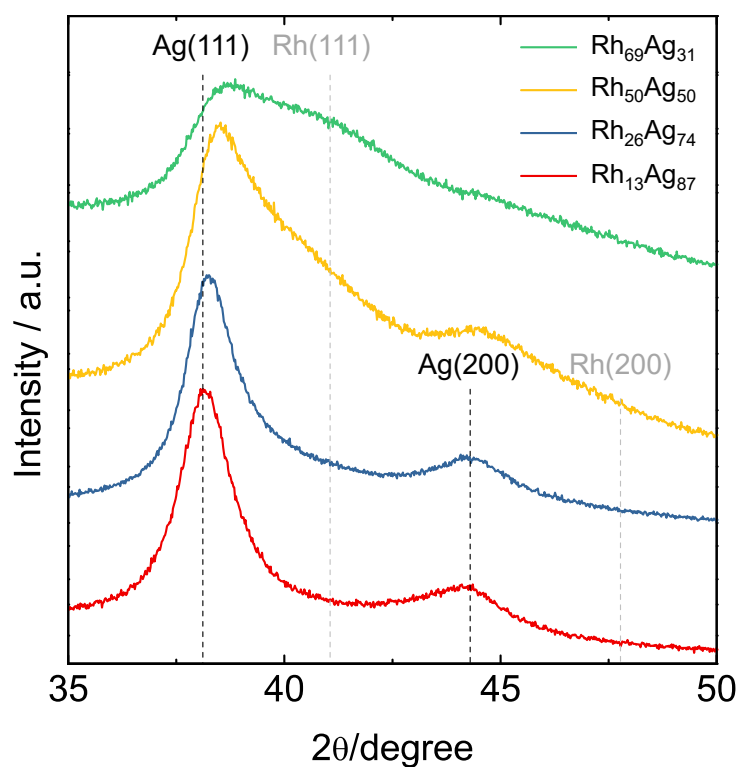


Fig. S7. XRD spectra of the RhAg NPs with different compositions. At low Rh contents (26% and below), the dominant peaks of the RhAg NPs align with those of pure Ag, indicating that homogeneous mixtures of Rh and Ag did not form. Peaks corresponding to pure Rh are not observed because Rh is present in amorphous phases. As the Rh content increases (50% and above), individual crystalline Rh domains develop; as a result, Rh peaks for the (111) planes (2θ of 41.06°) emerge, and the Ag(111) peaks slightly shift to larger angles.

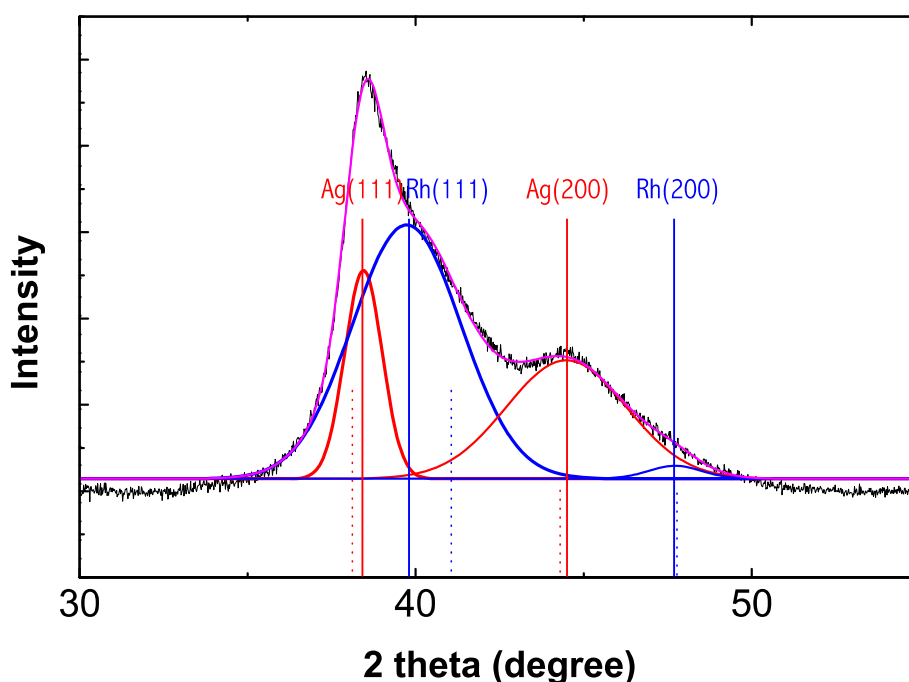


Fig. S8. XRD peak-deconvolution results of the Rh₅₀Ag₅₀ NP sample. Peak positions of the pure metals (JCPDS) are also shown as comparisons, and denoted by dashed lines: Ag(111) at 38.1°, Rh(111) at 41.1°, Ag(200) at 44.3°, and Rh(200) at 47.8°. While no shift was found for low Rh-content samples (Rh₁₃Ag₈₇ or Rh₂₆Ag₇₄ NPs), a small peak-shift was indeed observed for Rh-rich samples (Rh \geq 50%). We performed the XRD deconvolution analysis of the Rh₅₀Ag₅₀ sample. One can see that the Ag(111) peak is shifted by +0.3°, Rh(111) peak is shifted by -1.3°, and Ag(200) and Rh(200) peaks are negligibly shifted, all compared to JCPDS positions. Though the shifts are overall small, these indicate a sign that the “partial alloying” occurred at the nanoscale in the Rh₅₀Ag₅₀ sample. However, it is very important to note that lower Rh-content samples (Rh \leq 26%), which exhibits comparatively much higher H₂O₂ production rates, do not show any signs of alloying in XRD; thus, H₂O₂ productions in our samples are not a result of alloying. The key conclusions of the present study are still solid.

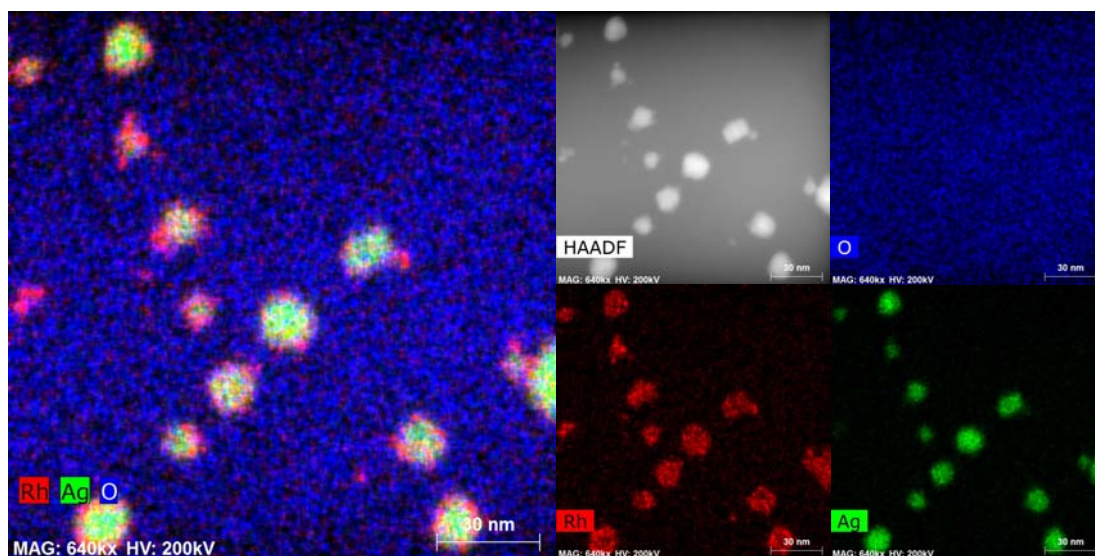


Fig. S9. The representative HAADF grayscale image and the corresponding EDS (RGB) maps of the collective Rh₂₆Ag₇₄ NPs. The qualitative elemental distributions of Rh, Ag, and O are represented in red, green, and blue, respectively. However, oxygen was observed at noise-level over the entire background; thus, it was extremely difficult to identify whether Rh is oxidized from EDS results.

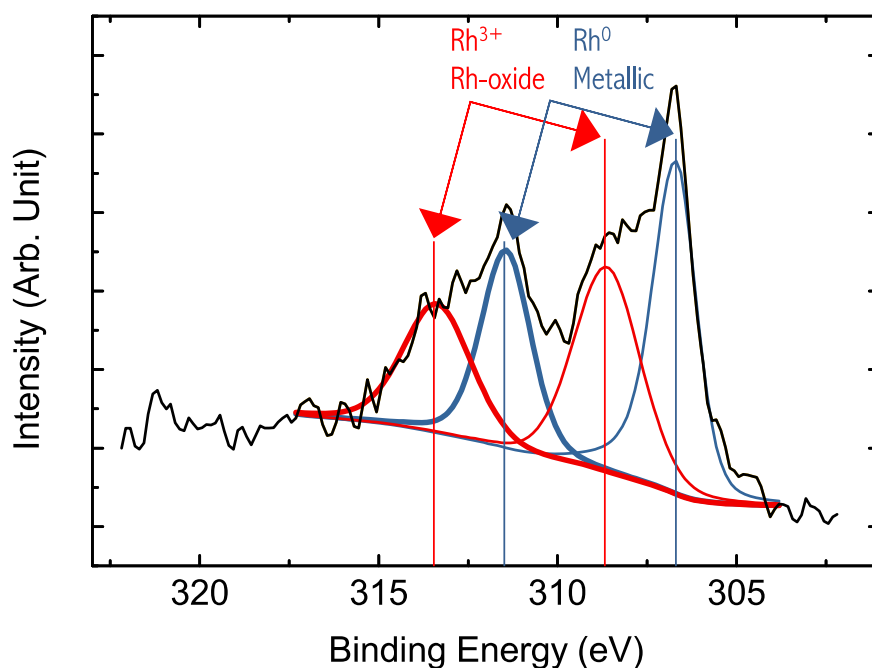


Fig. S10. XPS spectra and the deconvolution (curve-fitting) results of Rh 3d of Rh₂₆Ag₇₄. The peaks of Rh³⁺ and Rh⁰ are shown in red and blue, respectively. XPS is a suitable method to identify whether Rh is oxidized and, further, to quantify the degree of oxidation. Taking the Rh₂₆Ag₇₄ sample as an example, we observe and estimate approximately 46% Rh³⁺ peaks (as in Rh₂O₃), which indicates Rh is partially oxidized.

Table S5. A comparison of catalytic performance of unsupported and silica-supported Pd NP. All catalytic test conditions are identical: T, 20°C; P, 1 atm; reaction medium, 150 ml of a DI water mixture (20% ethanol, 0.9 mM KBr, and 0.03 M H₃PO₄); total flow rate, 22 ml/min; H₂/O₂, 1/10.

	Fresh Pd catalyst	Pd/SiO₂ catalyst (Change in %, compared to fresh catalyst)
Productivity (mmol g ⁻¹ h ⁻¹)	59	48 (-18%)
Selectivity (%)	39	36 (-7%)
H ₂ conversion (%)	11	7 (-36%)

Table S6. Catalytic performances of all the NPs investigated in the present work.

The cost-normalized productivity (CNP) was calculated to compare the cost-effectiveness of the developed catalyst materials. Reactions were carried out under the following conditions: T, 20°C; P, 1 atm; reaction medium, 150 ml of DI water mixture (20% ethanol, 0.9 mM KBr, 0.03 M H₃PO₄); reaction time, 1 h; total flow rate, 22 ml/min; H₂/O₂, 1/10. For Pd NPs, several literature values are also shown for comparison^{S7,S8,S9}.

Catalyst	H ₂ O ₂ productivity (mmol g _{cat} ⁻¹ h ⁻¹)	H ₂ O ₂ productivity (CNP, mmol S _{cat} ⁻¹ h ⁻¹)	H ₂ conversion (%)	H ₂ O ₂ selectivity (%)	
Pd NPs (Literature)	Pd (cube) ^{S8}	66	N/A	7	39.5
	Pd (cube) ^{S9}	86	N/A	10	30
	Pd (octa) ^{S10}	106	N/A	10.5	41.5
	Pd ^{S7}	31	N/A	29	21
Pd	59	1.8	11.7	39	
Ag	0	0	0	0	
Au	0	0	1.3	0	
Rh	0	0	0.4	0	
Ir	0	0	0.6	0	
Pt	20	0.7	10.9	4	
RhAg NPs	Rh ₅ Ag ₉₅	0	0	0.2	0
	Rh ₁₃ Ag ₈₇	67	13.3	3.2	62
	Rh ₂₆ Ag ₇₄	30	2.1	2.4	78
	Rh ₅₀ Ag ₅₀	8	0.3	5.1	16
	Rh ₆₉ Ag ₃₁	0	0	0.4	0
Rh ₄₆ Au ₅₄	56	1.3	3.0	37	
PtAu NPs	Pt ₈ Au ₉₂	103	2.6	9.0	39
	Pt ₂₈ Au ₇₂	300	8.0	28.0	36
	Pt ₄₂ Au ₅₈	237	6.6	21.9	13
Ir ₁₈ Ag ₈₂	13	0.8	2.9	18	
Ir ₁₀ Au ₉₀	0	0	5.6	0	

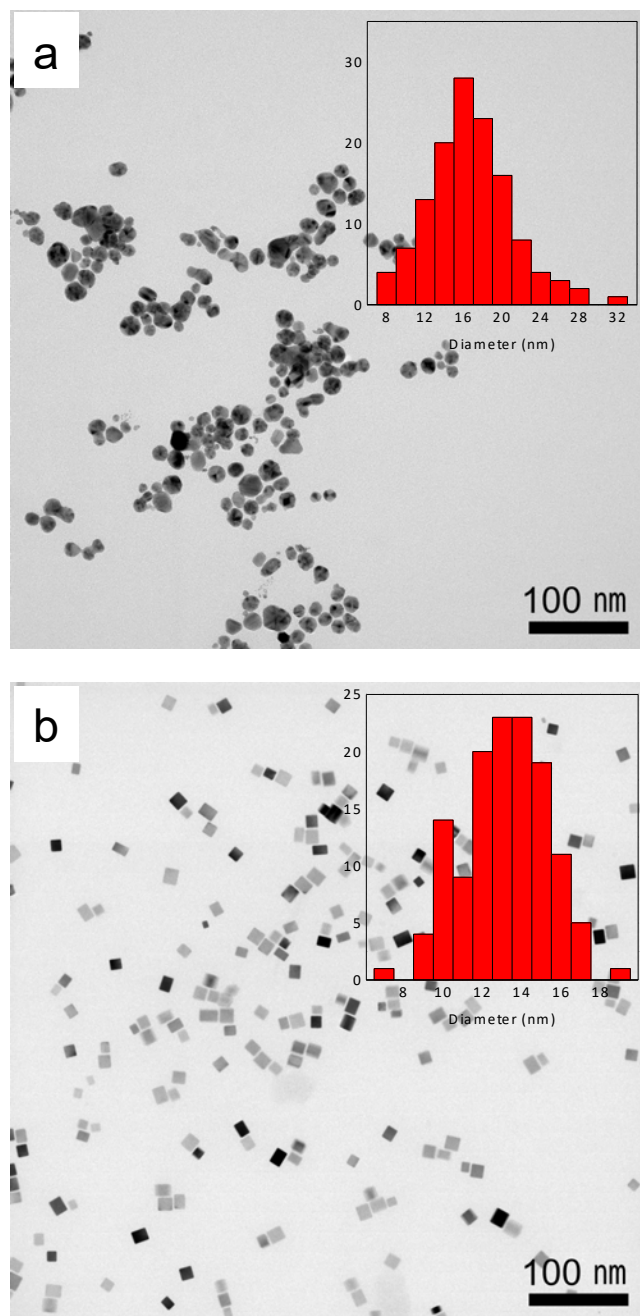


Fig. S11. TEM images of the (a) Rh₁₀Ag₉₀ NPs and (b) Pd NPs. While the RhAg NPs develop spherical shapes, the Pd NPs form perfect cube shapes with the (100) surfaces exposed. The particle size distributions are also shown in the inset of each image. Rh₁₀Ag₉₀ NPs synthesized from the polyol reduction method are primarily sphere-shaped with the average diameter (d) of 15.74nm, while Pd NPs are cube-shaped with the average side length (l) of 12.58nm. Given 1gram of metal loading, total surface area (S) can be calculated as follows: (1) S of Pd cube NPs: $N_{Pd} \times 6l^2 = (1\text{gram} / \rho_{Pd} \cdot l^3) \times 6l^2 = 3.76 \times 10^{19}$

(nm²), (2) *S* of Rh₁₀Ag₉₀ spherical NPs: $N_{\text{RhAg}} \times \pi d^2 = [1 \text{ gram} / \rho_{\text{RhAg}} \cdot (\pi d^3 / 6)] \times \pi d^2 = 3.57 \times 10^{19}$ (nm²), where N_{Pd} , N_{RhAg} is the number of Pd and RhAg NPs in total 1g metal loading, respectively, and ρ_{Pd} , ρ_{RhAg} is the effective density of Pd (12.68g/cm³) and Rh₁₀Ag₉₀ (10.68g/cm³), respectively. One can observe from the above comparisons that the cubed Pd NPs have a very similar surface area to our RhAg NPs (less than 5% difference) and therefore can serve as a great reference system. In contrast to the cubed Pd NPs, we observed that spherical Pd NPs could be formed only with a much smaller NP diameter ($d < 8$ nm); thus, direct comparisons of our samples with spherical Pd NPs are difficult, as the total surface areas differ too much.

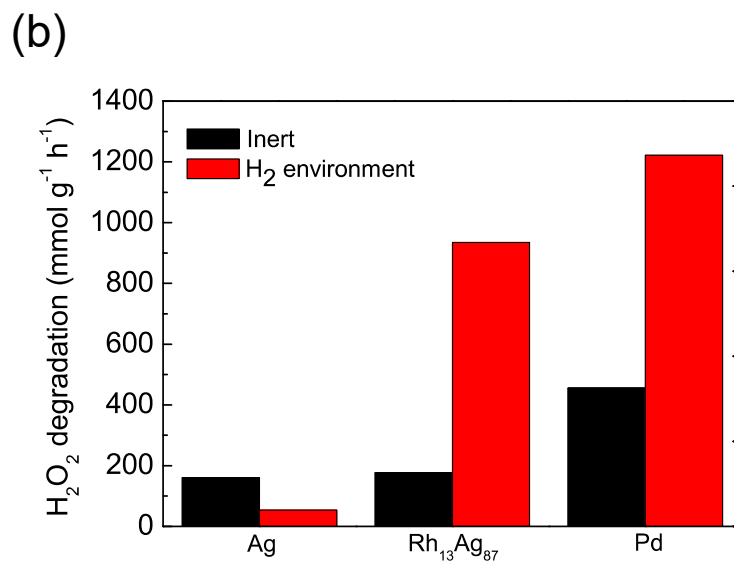
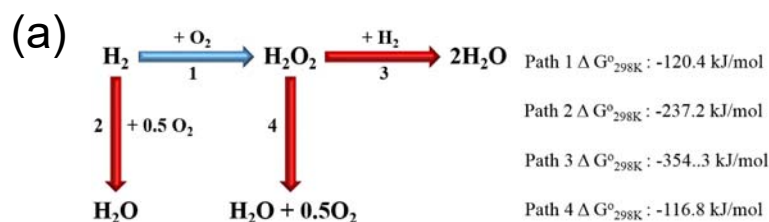


Fig. S12. H₂O₂ degradation tests of Rh₁₃Ag₈₇ NPs under both inert and H₂-containing atmospheres in comparisons to pure Ag and Pd NPs. (a) A schematic flow of direct H₂O₂ synthesis and degradation. Steps 3 and 4 represent H₂O₂ degradation under H₂-containing and inert environments, respectively. (b) H₂O₂ decomposition test results, shown in units of mmol g⁻¹ h⁻¹. The reaction conditions are as follows: T, 20°C; P, 1 atm; 1 ml of H₂O₂ (35 wt% in H₂O); reaction medium, 150 ml of a 0.03 M H₃PO₄ 20 vol.% ethanolic solution with 0.09 mM KBr; total flow rate, 22 ml/min; time, 1 h. For the hydrogenation reaction, H₂/N₂=1/10 was used.

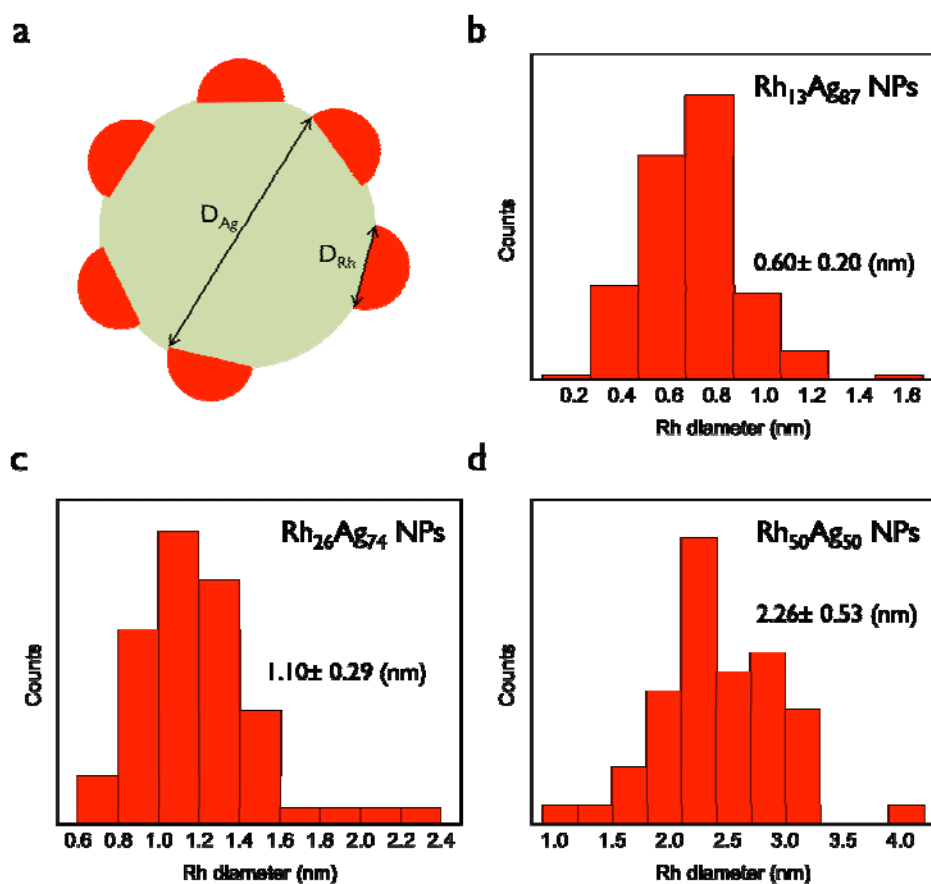


Fig. S13. A schematic of our representative NPs and Rh particle size distributions. **a**. A model schematic for estimating interfacial length. **b-d**. Histograms showing Rh particle size (diameter) distributions for $Rh_{13}Ag_{87}$, $Rh_{26}Ag_{74}$, and $Rh_{50}Ag_{50}$ NPs.

Table S7. Interfacial length estimations of RhAg NPs of different compositions. The diameter of Rh clusters is averaged over 100 samples. The numbers in the parentheses are values of standard deviations. The details of the model to estimate interfacial length are elaborated as follows.

Materials	D_{Rh} , nm	Interfacial length, 10^{20} nm/g _{cat}	Interfacial length (normalized to the largest)	Productivity, mmol/g _{cat} h	Productivity (normalized to the largest)
Rh ₁₃ Ag ₈₇ NPs	0.60 (± 0.20)	3.49 (± 1.16)	1.0	67.4	1.0
Rh ₂₆ Ag ₇₄ NPs	1.10 (± 0.29)	2.08 (± 0.55)	0.60	30.0	0.45
Rh ₅₀ Ag ₅₀ NPs	2.26 (± 0.53)	0.95 (± 0.22)	0.27	7.5	0.11

This model uses TEM-EDS images as key inputs. A schematic of the model is shown above in **Fig. S11**. We assume that Rh hemispheres are distributed on the spherical Ag cores. Let us define the following three parameters: ρ_{Rh} (Rh density)=12.4 (g/cm³), D_{Rh} (diameter of Rh hemispheres, in nm unit), N_{Rh} (number of Rh hemispheres in a given system).

- Given 1 gram of Rh_xAg_{1-x} NPs (x as Rh content), the total weight of Rh in the system can be equated as: $N_{Rh} (2\pi(D_{Rh}/2)^3/3) \rho_{Rh} = x$ (g) ... (1)
- Total interfacial length per gram of catalyst (nm/g_{cat}) = $N_{Rh} (\pi D_{Rh})$... (2)

Plugging (1) into (2), we can estimate total interfacial length as $12x/\rho_{Rh} D_{Rh}^2$ (in nm/g_{cat}).

We used the manually measured diameter statistics (histogram in Fig. S10). The statistical results reveal that the average cluster size increases with Rh content (0.60 (± 0.20) nm for Rh₁₃Ag₈₇ → 2.26 (± 0.53) nm for Rh₅₀Ag₅₀ NPs). This consequently leads to the decrease of interfacial length with increasing Rh content. This trend is consistent with the decrease of experimental H₂O₂ productivity with increasing Rh content. Comparing the correlations between productivity and interfacial length (in normalized scale), we noted that productivity of Rh₅₀Ag₅₀ NPs is much worse than what is expected from the interfacial length estimation, and this is likely due to the partial alloying in this sample, which further degrades the catalytic activity (**Fig. S12**).

O₂ dissociation on alloyed RhAg
: (111) surface

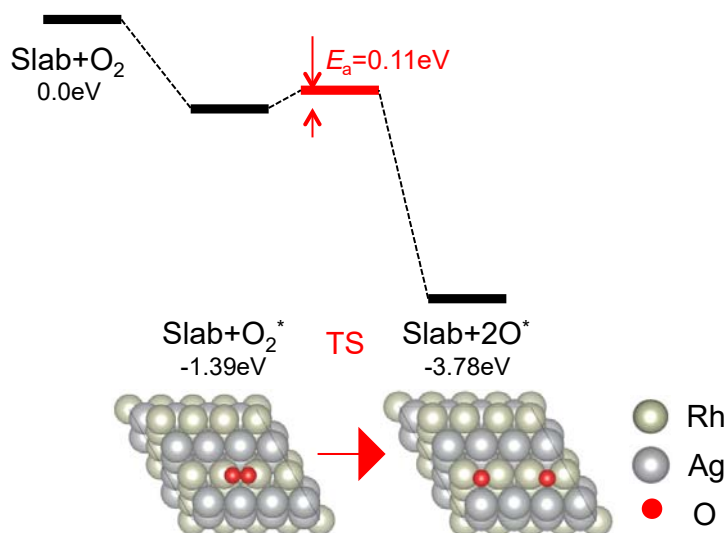


Fig. S14. DFT calculation results of O₂ dissociation energetics on the alloyed RhAg (111) surface. The O₂ dissociation barrier on alloyed (111) surface is found very small of ~0.11 eV, and thus O₂ molecules will easily be broken into O atomic species, which in turn indicates that H₂O₂ productions are highly unlikely to occur on the alloyed surface. These DFT calculations can adequately (at least partially) explain the substantial drop of H₂O₂ productivity for the Rh₅₀Ag₅₀ NPs in which the partial alloying of Rh and Ag elements are observed (67.4 mmol g⁻¹ h⁻¹ for Rh₁₃Ag₈₇ → 7.53 mmol g⁻¹ h⁻¹ for Rh₅₀Ag₅₀).

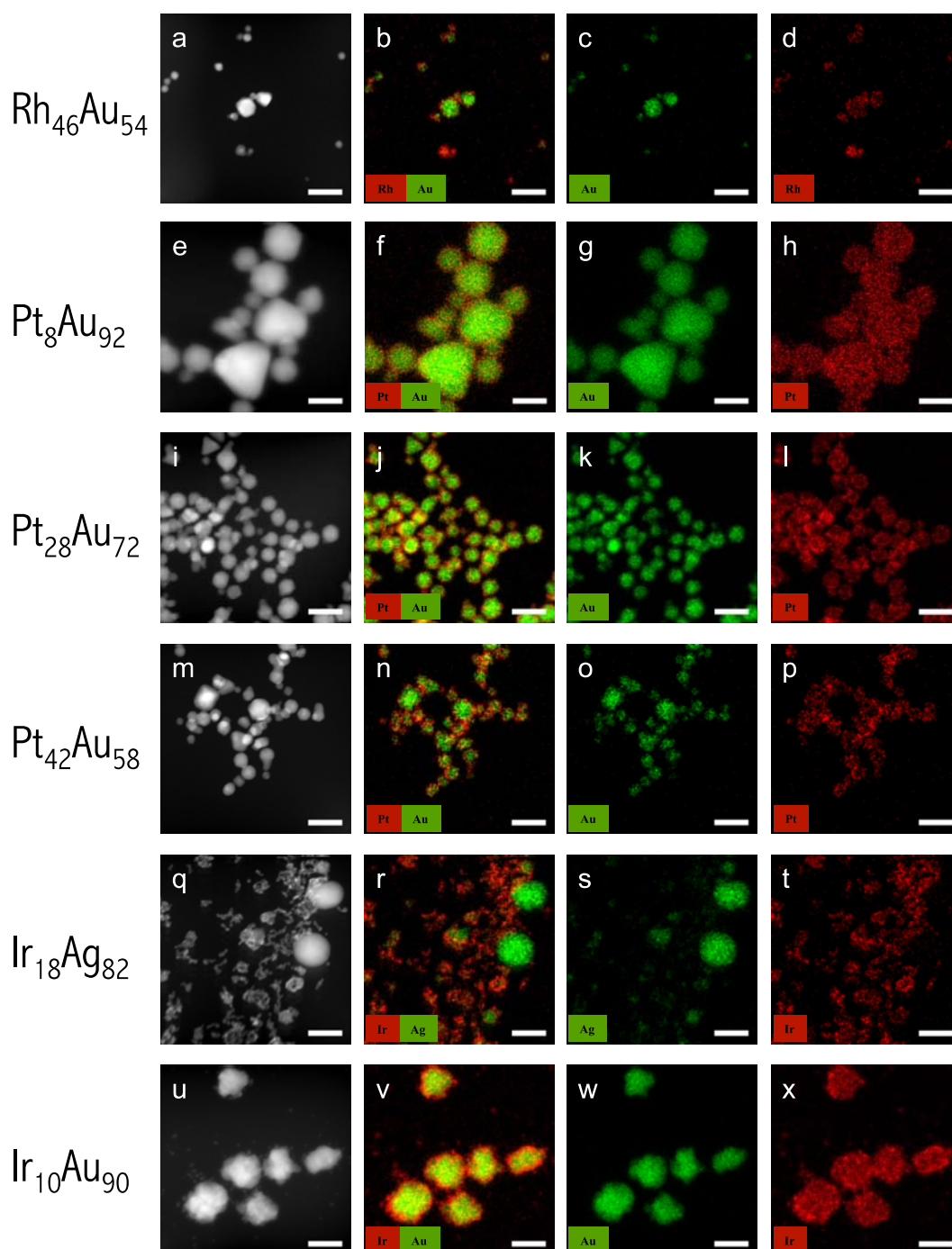


Fig. S15. Structural analysis of the RhAu, PtAu, IrAg, and IrAu NPs. The representative HAADF grayscale image and EDS (RGB) maps of the collective (a-d) Rh₄₆Au₅₄, (e-h) Pt₈Au₉₂, (i-l) Pt₂₈Au₇₂, (m-p) Pt₄₂Au₅₈, (q-t) Ir₁₈Ag₈₂, and (u-x) Ir₁₀Au₉₀ NPs. Scale bars in the images and maps represent 20 nm.

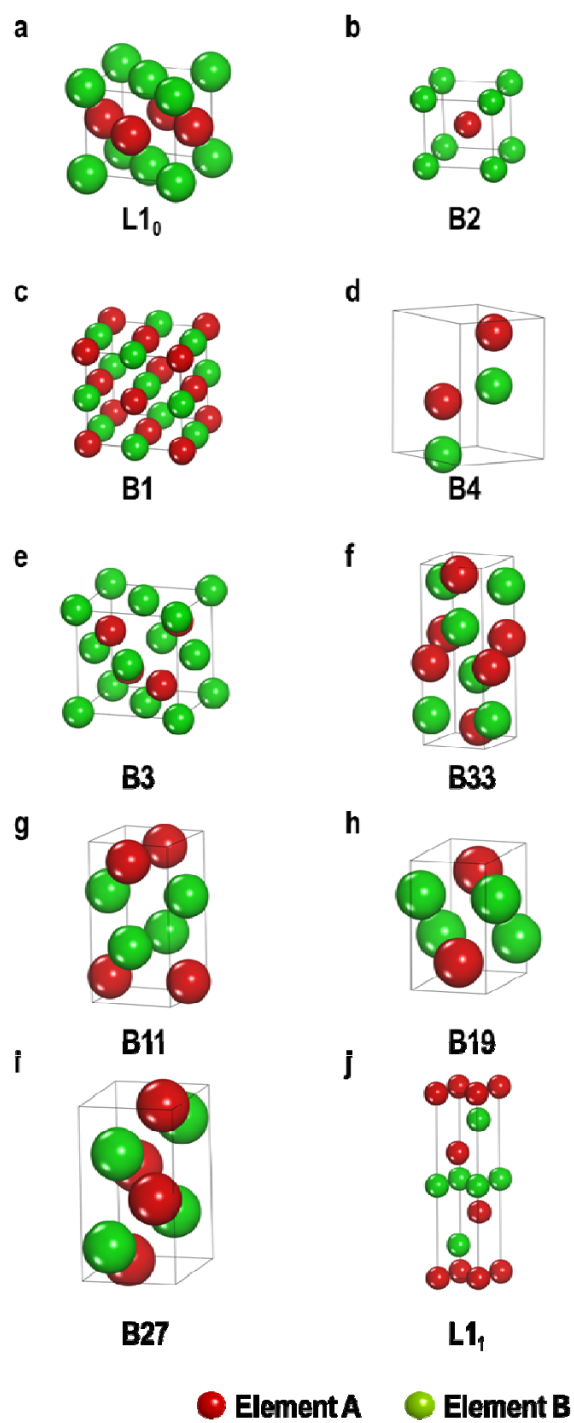


Fig. S16. Unitcell crystal structures of 10 possible thermodynamic phases of 1:1 binary alloy. (a) L1₀, (b) B2, (c) B1, (d) B4, (e) B3, (f) B33, (g) B11, (h) B19, (i) B27, and (j) L1₁.

	Sc	Ti	V	Cr	Mn	Fe	Co	Ni	Cu	Zn	Y	Zr	Nb	Mo	Tc	Ru	Rh	Pd	Ag	Cd	Lu	Hf	Ta	W	Re	Os	Ir	Pt	Au	Hg
Sc	0.00	0.86	0.98	1.04	0.50	0.55	-0.06	-0.42	0.02	-0.15	0.70	0.63	0.93	1.11	0.96	-0.46	-1.44	-1.19	0.04	0.09	0.69	0.74	1.01	1.28	0.84	-0.02	-1.43	-1.87	-1.01	0.07
Ti	0.86	0.00	0.22	0.08	-0.54	-0.75	-0.73	-0.73	-0.28	-0.38	0.35	0.05	0.12	-0.09	-0.54	-1.51	-1.49	-1.05	0.19	0.13	0.48	0.16	0.19	0.20	-0.78	-1.40	-1.70	-1.84	-0.77	0.29
V	0.98	0.22	0.00	-0.21	-0.62	-0.27	-0.20	-0.39	0.31	0.02	0.71	0.31	0.10	-0.28	-0.32	-0.47	-0.73	-0.36	0.83	0.53	0.61	0.25	0.04	-0.15	-0.72	-0.46	-1.01	-1.17	0.19	1.20
Cr	1.04	0.08	-0.21	0.00	0.01	0.30	0.28	0.67	0.82	0.47	0.60	0.26	0.07	0.07	0.54	0.27	-0.04	0.14	0.89	0.86	0.52	0.15	-0.10	0.04	0.07	0.44	-0.38	-0.31	0.22	1.11
Mn	0.50	-0.54	-0.62	0.01	0.00	0.11	0.12	-0.37	0.09	-0.09	0.11	-0.13	-0.31	0.23	0.62	-0.17	-0.62	-0.62	0.32	0.34	0.07	-0.34	-0.59	0.19	0.06	0.02	-0.50	-1.02	-0.35	0.66
Fe	0.55	-0.75	-0.27	0.30	0.11	0.00	-0.19	0.14	0.27	-0.02	0.36	-0.30	-0.04	0.39	0.49	0.30	-0.23	-0.19	0.68	0.69	0.35	-0.61	-0.29	0.42	0.17	0.37	0.03	-0.55	0.29	1.22
Co	-0.06	-0.73	-0.20	0.28	0.12	-0.19	0.00	0.02	0.38	0.12	-0.20	-0.53	-0.22	0.11	0.62	0.40	0.14	0.10	0.94	0.68	-0.44	-0.73	-0.19	0.17	0.17	0.43	0.10	-0.19	0.55	1.29
Ni	-0.42	-0.73	-0.39	0.67	-0.37	0.14	0.02	0.00	0.10	-0.48	-0.74	-0.71	-0.28	0.03	0.52	0.32	0.09	0.03	0.60	0.16	-0.94	-0.89	-0.16	0.14	0.15	0.44	0.06	-0.21	0.22	0.69
Cu	0.02	-0.28	0.31	0.82	0.09	0.27	0.38	0.10	0.00	-0.18	-0.51	-0.24	0.21	0.47	0.93	0.73	0.25	-0.27	0.22	0.18	-0.84	-0.20	0.27	0.76	0.76	1.11	1.88	-0.30	-0.08	0.70
Zn	-0.15	-0.38	0.02	0.47	-0.08	-0.02	0.12	-0.48	-0.18	0.00	-0.72	-0.53	-0.11	0.28	0.88	0.28	-0.76	-1.11	-0.10	0.18	-0.89	-0.37	0.07	0.68	0.84	0.93	-0.21	-1.12	-0.41	0.48
Y	0.70	0.35	0.71	0.60	0.11	0.36	-0.20	-0.74	-0.51	-0.72	0.00	0.09	0.87	0.87	0.83	-0.54	-1.68	-1.74	-0.67	-0.64	-0.01	0.22	1.00	1.08	0.92	-0.34	-1.57	-2.53	-1.75	-0.69
Zr	0.63	0.05	0.31	0.26	-0.13	-0.30	-0.53	-0.71	-0.24	-0.53	0.09	0.00	0.26	0.14	-0.27	-1.28	-1.53	-1.25	0.00	-0.09	0.17	0.10	0.29	0.51	-0.37	-1.03	-1.62	-2.22	-0.96	0.02
Nb	0.93	0.12	0.10	0.07	-0.31	-0.04	-0.22	-0.28	0.21	-0.11	0.87	0.26	0.00	-0.25	-0.24	-0.32	-0.81	-0.55	0.62	0.94	0.65	0.24	-0.04	-0.07	-0.54	-0.22	-1.02	-1.24	-0.13	0.82
Mo	1.11	-0.09	-0.28	0.07	0.23	0.39	0.11	0.03	0.47	0.29	0.87	0.14	-0.25	0.00	0.59	0.12	-0.38	0.10	1.09	1.07	0.99	0.02	-0.40	-0.03	0.20	0.15	-0.66	-0.62	0.62	1.67
Tc	0.96	-0.54	-0.32	0.54	0.62	0.49	0.62	0.52	0.93	0.88	0.83	-0.27	-0.24	0.59	0.00	0.25	0.21	1.08	1.39	1.33	0.64	-0.50	-0.57	0.57	1.00	0.51	0.10	0.28	1.22	2.13
Ru	-0.46	-1.51	-0.47	0.27	-0.17	0.30	0.40	0.32	0.73	0.29	-0.54	-1.28	-0.32	0.12	0.25	0.00	0.13	0.54	1.30	0.78	-0.88	-1.63	-0.65	0.10	0.03	0.27	-0.04	0.17	1.01	1.58
Rh	-1.44	-1.49	-0.73	-0.04	-0.62	-0.23	0.14	0.09	0.25	-0.76	-1.68	-1.53	-0.81	-0.38	0.21	0.13	0.00	0.14	0.44	-0.09	-2.00	-1.79	-0.95	-0.35	-0.13	0.82	0.70	-0.03	0.54	0.67
Pd	-1.19	-1.05	-0.36	0.14	-0.62	-0.19	0.10	0.03	-0.27	-1.11	-1.74	-1.25	-0.55	0.10	1.08	0.54	0.14	0.00	-0.09	-0.76	-1.94	-1.34	-0.69	0.28	0.50	0.84	0.40	-0.04	-0.16	-0.02
Ag	0.04	0.19	0.83	0.89	0.32	0.68	0.94	0.60	0.22	-0.10	-0.67	0.00	0.62	1.09	1.39	1.30	0.44	-0.09	0.00	-0.08	-0.67	0.14	0.84	1.47	1.45	1.86	0.51	0.11	-0.11	0.43
Cd	0.09	0.13	0.53	0.86	0.34	0.69	0.68	0.16	0.16	0.19	-0.64	-0.09	0.94	1.07	1.33	0.78	-0.09	-0.76	-0.08	0.00	-0.50	0.17	0.71	1.37	1.63	1.54	0.64	-0.55	-0.28	0.31
Lu	0.89	0.48	0.61	0.52	0.07	0.35	-0.44	-0.94	-0.64	-0.69	-0.01	0.17	0.65	0.99	0.84	-0.88	-2.00	-1.94	-0.67	-0.50	0.00	0.86	1.25	1.62	16.6	-0.30	-1.91	-2.66	-1.77	-0.59
Hf	0.74	0.16	0.25	0.15	-0.34	-0.61	-0.73	-0.89	-0.20	-0.37	0.22	0.10	0.24	0.02	-0.50	-1.63	-1.79	-1.34	0.14	0.17	0.66	0.00	0.30	0.36	-0.63	-1.40	-1.84	-2.31	-0.88	0.30
Ta	1.01	0.19	0.04	-0.10	-0.59	-0.29	-0.19	-0.16	0.27	0.07	1.00	0.29	-0.04	-0.40	-0.57	-0.65	-0.95	-0.69	0.84	0.71	1.25	0.30	0.00	-0.19	-0.86	-0.52	-1.20	-1.26	0.02	1.15
W	1.28	0.20	-0.15	0.04	0.19	0.42	0.17	0.14	0.76	0.68	1.08	0.51	-0.07	-0.03	0.57	0.10	-0.35	0.28	1.47	1.37	1.62	0.36	-0.19	0.00	0.19	0.89	-0.60	-0.30	1.03	1.86
Re	0.84	-0.78	-0.72	0.07	0.06	0.17	0.17	0.15	0.76	0.84	0.92	-0.37	-0.54	0.20	1.00	0.03	-0.13	0.50	1.45	1.63	16.6	-0.63	-0.86	0.19	0.00	1.18	-0.28	0.09	1.31	2.06
Os	-0.02	-1.40	-0.46	0.44	0.02	0.37	0.43	0.44	1.11	0.93	-0.34	-1.03	-0.22	0.15	0.51	0.27	0.82	0.84	1.86	1.54	-0.30	-1.40	-0.52	0.88	1.18	0.00	0.08	0.56	0.90	2.08
Ir	-1.43	-1.70	-1.01	-0.38	-0.50	0.03	0.10	0.06	1.89	-0.21	-1.57	-1.62	-1.02	-0.66	0.10	-0.04	0.70	0.40	0.81	0.64	-1.91	-1.84	-1.20	-0.60	-0.28	0.09	0.00	0.22	0.75	1.55
Pt	-1.87	-1.84	-1.17	-0.31	-1.02	-0.55	-0.19	-0.21	-0.30	-1.12	-2.53	-2.22	-1.24	-0.62	0.28	0.17	-0.03	-0.04	0.11	-0.55	-2.86	-2.31	-1.26	-0.30	0.09	0.56	0.22	0.00	0.16	0.40
Au	-1.01	-0.77	0.19	0.22	-0.35	0.29	0.55	0.22	-0.08	-0.41	-1.75	-0.98	-0.13	0.82	1.22	1.01	0.54	-0.16	-0.11	-0.28	-1.77	-0.88	0.02	1.03	1.31	0.90	0.75	0.16	0.00	0.38
Hg	0.07	0.29	1.20	1.11	0.86	1.22	1.29	0.88	0.70	0.48	-0.89	0.02	0.82	1.67	2.13	1.58	0.67	-0.02	0.43	0.31	-0.59	0.30	1.15	1.86	2.06	2.08	1.55	0.40	0.38	0.00

 : $E_f = 0$
 : $E_f < 0$
 : $E_f > 0$

Fig. S17. DFT-computed formation energies (E_f) of 435 binary alloys composed of two transition metals (in periods IV, V, VI). For each elemental combination, E_f of all 10 thermodynamic phases were compared, and only the most stable phase was presented. Boxes in blue, red, black represent “ $E_f < 0$ ”, “ $E_f > 0$ ”, and “ $E_f = 0$ ”, respectively.

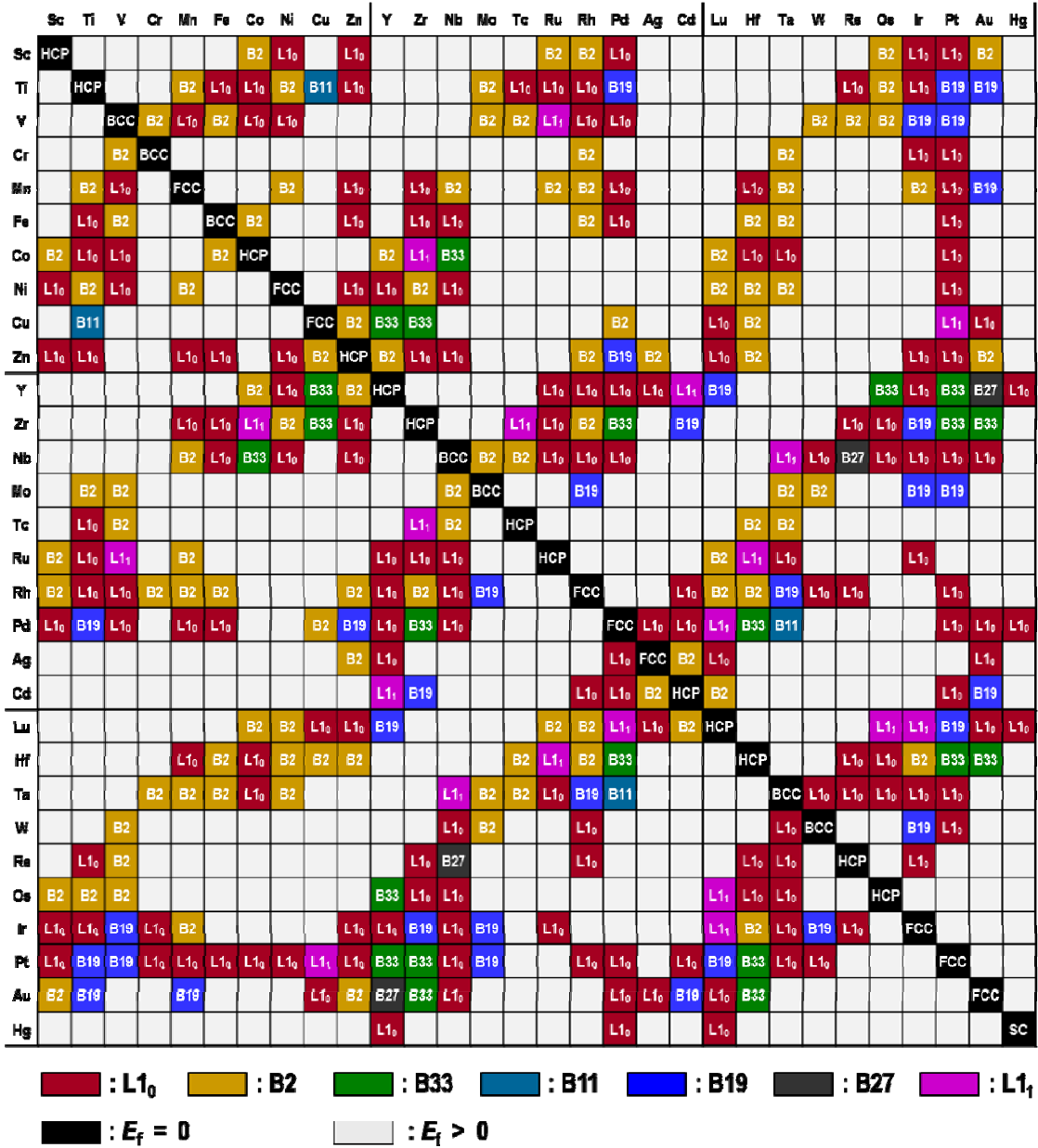


Fig. S18. The most stable thermodynamic phase for 183 miscible elemental combinations (i.e., $E_f < 0$) as well as pure metals.

Table S8. The number of elemental combinations in each classified phase for 183 miscible cases, and 252 immiscible ones.

Thermodynamic phase		Number of elemental combinations
Miscible alloy	AuCu (L1₀)	86 (20 %)
	CsCl (B2)	55 (12 %)
	NaCl (B1)	0 (0 %)
	Wurtzite (B4)	0 (0 %)
	Zinc blende (B3)	0 (0 %)
	CrB (B33)	11 (3 %)
	TiCu (B11)	2 (0.5%)
	CdAu (B19)	17 (4%)
	FeB (B27)	2 (0.5%)
	CuPt (L1_i)	10 (2%)
Immiscible alloy		252 (58%)
Total		435 (100%)

Table S9. Comparisons of catalytic test conditions (pressure, used catalyst weight, and H₂ flow rate) that can affect H₂ conversion between ours and selected literatures. Literatures here report a very high level of H₂ conversions (almost complete conversions). Cells shaded in gray color signify the more favorable conditions for H₂ conversions, compared to our own experiments, i.e. higher pressure, larger catalyst weight, lower H₂ flow rate. We observe that experiments were carried out in much higher pressure conditions (>10atm) in two articles of Park et al. and Burato et al.^{S10,S11}, which highly likely has led to much enhanced H₂ conversions. As for the other articles of Samanta et al. and Choudhary et al.^{S12,S13}, comparatively much larger catalyst weight ($\geq 10\text{mg}$) or lower H₂ flow rate may adequately account for such high conversion values.

Materials	Pressure condition	Used catalyst weight (mg)	H ₂ flow rate	References
Our new catalysts (RhAg, RhAu, PtAu)	1 atm	5–6.5mg (RhAg, RhAu); 1.7mg (PtAu)	2.0 (ml/min)	Not applicable
Pd/SBA-15	10atm	1000 (total) \times 0.5% (Pd loading wt%) =5mg	12.6 (ml/min)	[S10]
Pd/SiO ₂	19.7atm	50 \times 1% (Pd loading wt%) =0.5mg	Not available	[S11]
Pd/SiO ₂	1 atm	500 \times 2.5% (Pd loading wt%)=12.5mg	0.7 (cm ³ /min)	[S12]
PdO/Al ₂ O ₃	0.94atm	100 \times 10% (Pd loading wt%) =10mg	3.0 (cm ³ /min)	[S13]

References

- (S1) Li, J.; Ishihara, T.; Yoshizawa, K. Theoretical Study of the Decomposition and Hydrogenation of H₂O₂ on Pd and Au@Pd Surfaces: Understanding toward High Selectivity of H₂O₂ Synthesis. *J. Phys. Chem. C* **2011**, *115*, 7392-7398.
- (S2) Seo, D.-H.; Shin, H.; Kang, K.; Kim, H.; Han, S. S. First-Principles Design of Hydrogen Dissociation Catalysts Based on Isoelectronic Metal Solid Solutions. *J. Phys. Chem. Lett.* **2014**, *5*, 1819-1824.
- (S3) Fajin, J. S. C.; Cordeiro, M. N. D. S.; Gomes, J. R. B. On the Theoretical Understanding of the Unexpected O₂ Activation by Nanoporous Gold. *Chem. Commun.* **2011**, *47*, 8403-8405.
- (S4) Xu, Y.; Mavrikakis, M. Adsorption and Dissociation of O₂ on Ir(111). *J. Chem. Phys.* **2002**, *116*, 10846-10853.
- (S5) Ham, H. C.; Hwang, G. S.; Han, J.; Nam, S. W.; Lim, T. H. On the Role of Pd Ensembles in Selective H₂O₂ Formation on PdAu Alloys. *J. Phys. Chem. C* **2009**, *113*, 12943-12945.
- (S6) Verhallen, P. T. H. M.; Oomen, L. J. P.; Elsen, A. J. J. M. v. d.; Fortuin, J. M. H. The Diffusion Coefficients of Helium, Hydrogen, Oxygen and Nitrogen in Water Determined from the Permeability of a Stagnant Liquid Layer in the Quasi-s. *Chem. Eng. Sci.* **1984**, *39*, 1535-1541.
- (S7) Edwards, J. K.; Hutchings, G. J. Palladium and Gold-Palladium Catalysts for the Direct Synthesis of Hydrogen Peroxide. *Angew. Chem. Int. Ed.* **2008**, *47*, 9192-9198.
- (S8) Kim, S.; Lee, D.-W.; Lee, K.-Y. Direct Synthesis of Hydrogen Peroxide from Hydrogen and Oxygen over Single-Crystal Cubic Palladium on Silica Catalysts. *J. Mol. Catal. A: Chem.* **2014**, *383*, 64-69.
- (S9) Kim, S.; Lee, D.-W.; Lee, K.-Y. Shape-Dependent Catalytic Activity of Palladium Nanoparticles for the Direct Synthesis of Hydrogen Peroxide from Hydrogen and Oxygen. *J. Mol. Catal. A: Chem.* **2014**, *391*, 48-54.
- (S10) Park, S.; Kim, T. J.; Chung, Y.-M.; Oh, S.-H.; Song, I. K. Direct Synthesis of Hydrogen Peroxide from Hydrogen and Oxygen over Palladium Catalyst Supported on SO₃H-Functionalized SBA-15. *Catal. Lett.* **2009**, *130*, 296-300.
- (S11) Burato, C.; Campestrini, S.; Han, Y.-F.; Canton, P.; Centomo, P.; Canu, P.; Corain, B. Chemoselective and Re-usable Heterogeneous Catalysts for the Direct Synthesis of Hydrogen Peroxide in the Liquid Phase under Non-explosive Conditions and in the Absence of Chemoselectivity Enhancers. *Appl. Catal. A: Gen* **2009**, *358*, 224-231.
- (S12) Samanta, C.; Choudary, V. R. Direct Formation of H₂O₂ from H₂ and O₂ and Decomposition/Hydrogenation of H₂O₂ in Aqueous Acidic Reaction Medium over Halide-Containing Pd/SiO₂ Catalytic System. *Catal. Commun.* **2007**, *8*, 2222-2228.
- (S13) Choudhary, V. R.; Jana, P. Direct Oxidation of H₂ to H₂O₂ over PdO/Al₂O₃ Catalysts in Aqueous Acidic Medium: Influence on H₂O₂ Formation of Pd Loading,

Calcination Temperature and Reduction of Catalyst and Presence of Halide Anions. *Catal. Commun.* **2008**, *9*, 2371-2375.